Extending the operating range of axial turbines with the protrusion of radially adjustable flat plates: An experimental investigation

Shahab Shiraghaee [a],[*], Joel Sundström [a], Mehrdad Raisee [b], Michel J. Cervantes [a]

[a] Department of Engineering Sciences and Mathematics, Luleå University of Technology, Luleå, Sweden
[b] Hydraulic Machinery Research Institute, School of Mechanical Engineering, College of Engineering, University of Tehran, Tehran, Iran

ARTICLE INFO

ABSTRACT

The implementation of hydropower to stabilize electrical grids dictates more frequent off-design operations of these renewable energy resources. Flow instabilities under such conditions reduce the efficiency of hydro turbines. Part-load operation is particularly detrimental since the development of a rotating vortical structure termed rotating vortex rope (RVR) in the draft tube leads to periodic pressure pulsations that jeopardize turbine performance. This paper experimentally explores a novel solution involving the protrusion of flat plates into the turbine draft tube. Three flat plates equally separated by 120° were vertically installed on the draft tube wall. The plates were protruded up to 83% of the draft tube local radius under four different part-load conditions. Their impact was observed through time-resolved pressure measurements in the draft tube and vaneless space, as well as efficiency measurements. The results demonstrated successful RVR mitigation, achieving a maximum 85% reduction in pressure oscillation amplitudes. Protruding flat plates disrupted RVR periodicity and coherence, confining its orbit to the draft tube center. This approach proved particularly effective at lower part-load conditions, enhancing turbine hydraulic efficiency by increasing torque extraction. Reducing the adverse effects under part load, the proposed method appears promising in extending the operational range of hydraulic turbines.

1. Introduction

Over the recent years, the environmental and sustainability concerns associated with electricity production have incentivized countries to seek and implement fossil-free solutions. This has paved the way for increased integration of clean, renewable energy sources in the power grid, which is expected to increase further in the future. Hydropower is a critical component in the development and expansion of a clean and sustainable production grid. As of 2018, hydropower comprised about 50% of the renewable electricity generation sources worldwide [1]. Moreover, hydropower can rapidly respond to the market's shifting demands. Thus, it is deemed an ideal tool for providing grid stability by complementing the intermittent production of wind and solar sources [2]. Consequently, more flexibility is expected from hydraulic turbines to operate more frequently away from their optimum design point, called the best efficiency point (BEP). The operation under off-design conditions undermines the performance of hydro turbines and jeopardizes their sustainable use.

When a single-regulated turbine of Francis or propeller type operates under partial discharge known as part load (PL), low-frequency oscillations relative to the runner frequency appear in the draft tube, dominating the hydraulic conduit [3]. The flow developed under such conditions affects the turbine's power output, thus reducing the efficiency [4]. Under the PL conditions, the guide vane opening angle is small, which means that the flow enters the runner at high swirls [5–7]. In single-regulated turbines, however, this swirl cannot be extracted due to the fixed angle of the runner blades. As a result, a residual swirl enters the draft tube. Ideally, the flow is supposed to leave the runner blades in the axial direction to achieve the highest efficiency at the BEP operation [8]. A consequence of the residual swirl entering the draft tube under PL condition is a region close to the wall exhibiting a large tangential velocity, which in turn causes the formation of a low-velocity region in the center. The high shear between the recirculating and swirling flow region may lead to the formation of a vortical structure that is typically termed rotating vortex rope (RVR) or precessing vortex core (PVC) [9]. Here, the former will be used to address the vortical flow structure

---

* Corresponding author.
E-mail addresses: shahab.shiraghaee@ltu.se (S. Shiraghaee), joel.sundstrom@ltu.se (J. Sundström), mraisee@ut.ac.ir (M. Raisee), Michel.Cervantes@ltu.se (M.J. Cervantes).

prevailing in the draft tube at PL. The RVR precession in the draft tube increases pressure oscillations, aggravates draft tube losses, and induces periodic loadings in the rotational and axial directions [9–11]. While the rotating (asynchronous) mode of these periodic oscillations originates from the RVR circulation, the axial or plunging (synchronous) mode of the latter appears due to the interaction between the RVR and the draft tube elbow [11–13]. RVR precession occurs at a frequency range between 0.15 and 0.4 of the runner rotational frequency, depending on the prevailing PL conditions and the investigated turbine characteristics [14–16]. The vortical flow with low-frequency precession is the primary source of PL pressure oscillations in the turbine draft tube [17]. Therefore, with the growing demand for the operation of hydraulic turbines under PL conditions, it is essential to find solutions addressing the adverse effects of the RVR. This way, the negative impact of the PL operation on turbine performance and lifetime can be reduced. Ideally, hydraulic turbines should operate smoothly and efficiently at any flow rate.

Different means to mitigate the RVR have been proposed throughout the years. The investigated RVR mitigation methods can be classified as fluid-based and geometry-based [18]. Fluid-based methods include water or air injection into the draft tube from different locations. Water injection has been successfully used in many investigations to mitigate the RVR-induced pressure pulsations and unify the pressure distribution in the draft tube [19–23]. Bosioc et al. [20] showed that axial injection from the runner cone in a model-sized, free-spinning swirl generator improves the pressure recovery along the draft tube. However, while the rotating mode of the RVR-induced pressure oscillations was mitigated in the draft tube using axial water injection, the plunging mode was aggravated. Nowadays, air injection is a widely adopted method with mixed results [8]. Aside from air injection at low flow rates, most fluid-based approaches are entailed by some efficiency losses [24].

Various geometrical modifications have been proposed with diverse performance mechanisms. Many of these modifications are applied to the shape and design parameters of the runner or draft tube cone to ensure a more uniform cross-sectional pressure distribution in the draft tube [25–28]. Another type of geometrical modification is imposed in the form of installations and extensions on the draft tube wall or the runner conical part [29–40]. Wall installations include J-grooves, baffles, fins, adjustable draft tube guide vanes, and rod protrusions. The installation of J-grooves in the draft tube is aimed to straighten the swirling flow, and the performance of such structures has been studied both experimentally and numerically [40,41]. Anup et al. [33] showed that J-grooves reduced the swirl strength in the draft tube. Thus, the backflow region in the center became narrower. The smaller vortex size reduced the amplitude of harmful pressure oscillations by approximately 50% while reducing the turbine efficiency by only 0.7%. J-grooves effectively suppress the swirling flow while inducing a minimal deterioration of the efficiency [8]. Chen et al. [34] numerically investigated J-grooves installed in the draft tube. Studying different shapes, they found that the increase of the J-groove length results in a magnified suppression of the swirling flow while amplifying the draft tube losses by up to 10% compared to the case with no J-grooves. However, the installation had no impact on the RVR frequency. Zhou et al. [35] studied different arrangements of baffles in the draft tube. They showed that a decrease of approximately 60% occurs in the RVR-induced pressure fluctuations due to the shrinkage of the stagnant zone, which is caused by the flow redirection to the draft tube center. Installing adjustable draft tube guide vanes (DTGV) is another technique that can achieve effective RVR mitigation by aligning and restricting the vortex core in the draft tube center [36]. Experimental validations of the latter concept in a 1:5.1 model of a high-head Francis turbine showed that its adverse effects on turbine performance under the PL operation were only about a 0.5% decrement in the hydraulic efficiency. Furthermore, the angle of DTGV installation had no added favorable impact on the RVR mitigation, and a vertical configuration was found to be the most efficient [37,38]. Shiraghaee et al. [39] investigated RVR

mitigation on a scaled-down turbine with variable-length cylindrical rod protrusion. The RVR-induced pressure oscillations were mitigated both in the rotating and plunging modes, with maximum reductions of 77% and 61%, respectively. Moreover, an optimum protrusion length was found where the highest mitigation was obtained. The same concept was also investigated on a 1:3.875 scaled model of the U9 Kaplan turbine under different PL conditions [42]. The obtained optimum protrusion lengths varied between the investigated operating conditions, while the optimum mitigation specific to each condition ranged from 10% to 85%.

DTGVs proved effective in mitigating the RVR under the PL with minimal performance losses. However, they demonstrated better mitigation under the lower PL condition than that closer to the BEP. On the other hand, the concept of rod protrusion does not offer the same mitigation levels as the latter; nevertheless, its adjustability means that it can be used over a wide range of operating conditions and actively optimized with the implementation of a feedback-loop controller. Thus, a successful combination of the two methods can provide high mitigation and improved performance while extending the operational range of the turbine under PL operation through adaptive protrusion. The current study investigates the effect of radially adjustable flat plates -protruded in the draft tube of a propeller turbine- on the pressure oscillations and turbine performance under PL conditions. The concept of using fixed guide vanes in the draft tube, as investigated in Ref. [38], is combined with that of the variable-length rod protrusion introduced in Ref. [39]. For this purpose, an arrangement of three flat plates is chosen for the draft tube insertion as the latter design was shown effective by Joy et al. [36]. The plates are protruded at variable spans under a range of PL operations. The pressure oscillations are captured and analyzed based on time-resolved pressure measurements performed at two sections along the draft tube and in the vaneless space. Also, efficiency measurements are performed to investigate how the mitigation method impacts the turbine performance.

The layout of the paper is organized as follows. First, the experimental setup used to conduct the experiments is described along with the specifications of the turbine model, sensors, mitigation apparatus, and data acquisition system. A description of the investigated operating conditions and the order of the measurements are also included in this section. Next, the tools developed to analyze the captured data are elaborated upon for the mean flow parameters and the time-resolved pressure data. In the results section, the repeatability of the test rig operational parameters, as well as the obtained pressure amplitudes, are first investigated. Then, the impact of flat-plate protrusion is quantified on the amplitude of the pressure oscillations through spectral analyses. Afterward, the underlying mitigation mechanisms are assessed with the help of pressure data phase-averaging and statistical analyses. Finally, the impact of the flat-plate protrusion system on the turbine's performance is scrutinized through observation of the efficiency and assessment of the losses.

2. Experimental apparatus

2.1. Test rig

The experimental setup used in the present investigation was a scaled-down model of the Porjus U9 Kaplan turbine with a scaling ratio of 98/1550. The prototype is installed along the Luleå river (Norrbotten, Sweden). It operates at a head of 55 m, producing 10 MW of electricity at a maximum flow rate of about 25 m^3/s. The draft tube in the model turbine is geometrically similar to that of the prototype, with a cone half-apex angle of 6.3°. The distributer in the spiral casing consists of 10 adjustable guide vanes. A 3-D printed runner with six fixed blades at an angle of 0.8° was installed in the test setup to rotate in the clockwise direction. This runner had a diameter of D = 98 mm and used the U9 turbine as a base design. However, the blades were slightly thickened, and the hub was modified to preserve the runner's structural integrity and facilitate printing. The test rig was installed on a closed-loop circuit,

as shown in Fig. 1.

A Grundfos TP65-120/2 A-F-A-B QQE centrifugal pump provided flow rates of up to Q = 10 l/s in the hydraulic circuit. Given the fixed blade angles of the runner, the turbine acts as a single-regulated machine, i.e., a propeller. A *Magnetic brake system* MBL-3.75 magnetic brake was installed on the turbine shaft to apply the loads, simulating the function of a generator. A Programmable logic controller (PLC) unit was developed and implemented to set the operating conditions of interest based on the readings of the global flow parameters. The net head (H) and the runner rotational frequency (n) were kept constants for all measurements at $H = 0.3$ m and $f_n = 10$ Hz, respectively. The net head was calculated based on Eq. (1) as follows:

$$H = \frac{\Delta P}{\rho g} + \frac{Q^2}{2g}\left(\frac{1}{A_1^2} - \frac{1}{A_2^2}\right) \tag{1}$$

where ΔP, ρ, and g denote the pressure difference between upstream and downstream of the turbine, working fluid density, and gravitational acceleration, respectively. A_1 and A_2 are the cross-section area of the waterway at the upstream and downstream differential pressure measurement sections, respectively. The pump rotational speed was adjusted to provide a constant head, whereas the magnetic brake was used to achieve a constant runner rotational frequency. Thus, constant values of $n_{ed} = nD/\sqrt{gH}$ were provided for the values of $Q_{ed} = Q/D^2\sqrt{gH}$ corresponding to each operating point. The operation of the test rig and the plate-protrusion device will be further elaborated in section 2.3.

2.2. Flat-plate protrusion setup

Three flat plates with rounded leading and trailing edges, a chord length of 0.63D, and a thickness of 0.02D were installed around the draft tube in an equally separated arrangement. Fig. 2 displays a view of the elbow draft tube and the relative location and dimensions of the flat plates. The leading edges of all the plates were located 0.1D below the runner cone and 0.33D above the elbow bend to protrude at adjustable lengths into the draft tube. The number and dimensions of the

protruding plates were chosen based on the results from the investigation of DTGVs in Ref. [36]. Therein, an optimum design consisting of three plates was suggested to be installed immediately below the runner hub's lower end. In addition, small chord lengths did not show significant RVR mitigations. In the present study, a large plate chord was chosen to cover the distance between the runner hub and the elbow bend. This ensures a significant impact of the concept without the need for optimizing the dimensions. However, the physical limitations imposed by the presence of the spiral casing block and elbow bend block (as shown in Fig. 1) only allowed a wall installation with a chord length of 0.63D located 0.1D below the runner. The plates were installed aligned with the draft tube axis and were inserted at equal lengths ranging from 0 to 83% of the draft tube radius at the bottom ($R_{DT} = 0.62D$) of the plates.

Three LinMot ps01-23x80 linear motors were used to provide the linear force required for the movement of the plates. Under each operating point, a series of protrusion lengths were investigated with an increment interval of $\Delta L \approx 0.08\ R_{DT}$.

2.3. Measurement and instrumentation

A total of six pressure sensors were installed on the draft tube wall at two sections (see sections A and B in Fig. 2). The axial locations of these sections were coincident with the leading and trailing edges of the flat plates. Sensors P_1, P_2, and P_3 were installed at section A, and the remaining three were installed at section B. The pressure sensors at each section were separated by 120° to enable the decomposition of the recorded signals into plunging and rotating components, as further elaborated in section 3.2. Another pressure sensor was installed in the vaneless space of the turbine head cover to observe the oscillations and their intensity upstream of the turbine moving parts. The turbine differential pressure, ΔP, was recorded using a Honeywell FP2000 differential pressure sensor, and the volumetric flow rate was measured using a Krohne Optiflux 2100 electromagnetic flowmeter. Since the turbine runner was 3-D printed using a plastic resin, and since the inherent inertia of the magnetic brake was small, the runner angular frequency in the original configuration of the runner/magnetic brake was susceptible
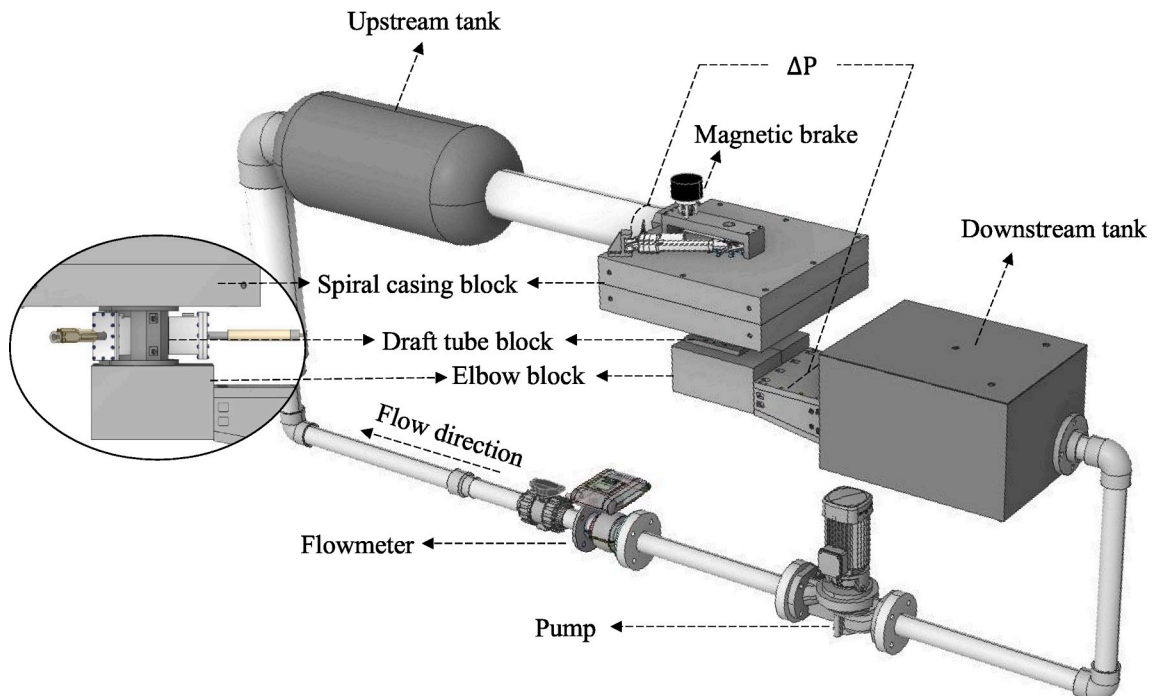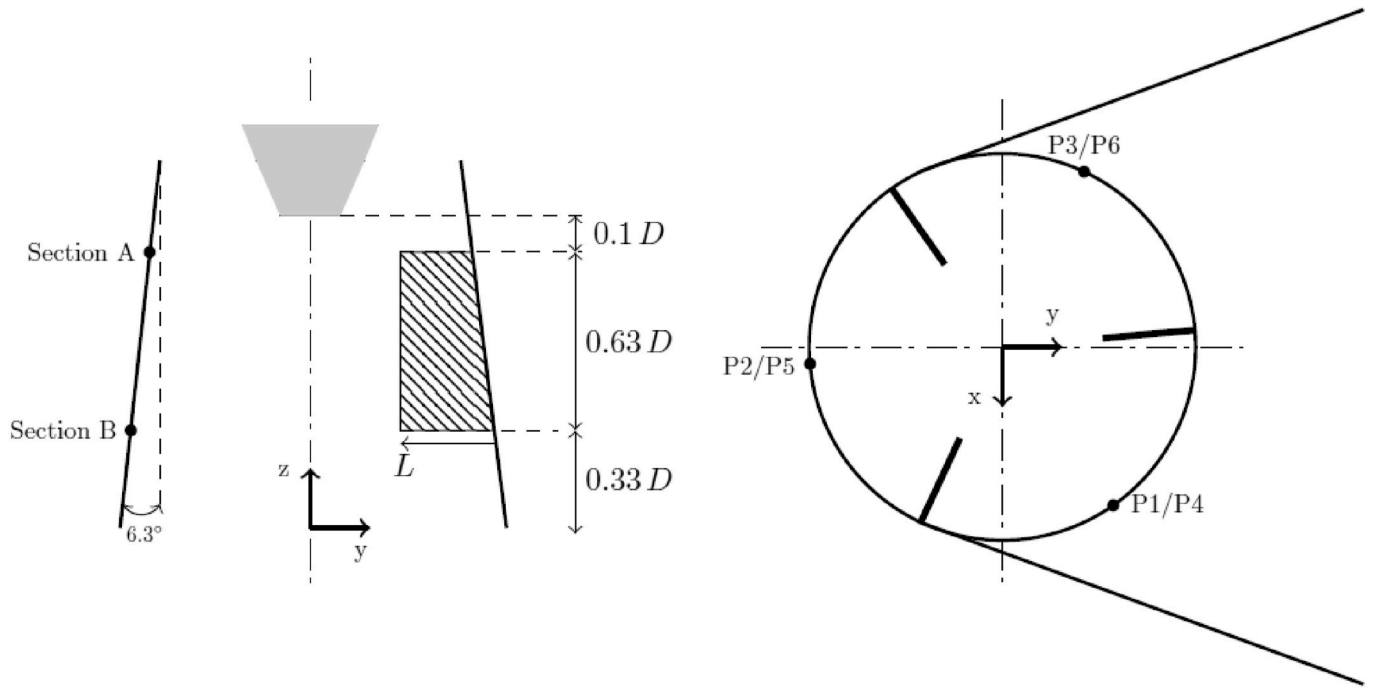

Fig. 1. Schematic view of the test rig. The small figure shows the respective location of the spiral casing block, elbow bend block, and draft tube block with the protrusion setup installed on the wall.

Fig. 2. Schematic of the turbine draft tube with the measurement and plate locations. The plates are installed 0.33 D above the elbow bend. Sensors P_1, P_2, and P_3 are located in section A while P_4, P_5, and P_6 are installed at section B.

to small variations in the turbine torque. As a remedy to reduce the sensitivity of the setup to small variations in the turbine torque, a 10 mm high, 200 mm diameter steel flywheel was installed above the magnetic brake. This configuration increased the moment of inertia by a factor of approximately 40. Close to the rim of the flywheel, 50 equally spaced holes had been drilled to measure the turbine runner's rotational speed. An Omron Transmissive photomicrosensor was used to measure the passage of the holes. The pulse-train signal of the photomicrosensor was converted to an analog signal using a Brodersen PXF-20 frequency to analog converter.

The mechanical torque was measured using an HBM T22 Torque transducer mounted on the shaft below the magnetic brake. Thus, the turbine efficiency could be measured under the different conditions using Eq. (2):

$$\eta = \frac{T\omega}{\rho gHQ} \tag{2}$$

Table 1
The sensors used in the experiments with their descriptions and uncertainties.

Measured variable	Sensor type	location	Range	Accuracy
$P_1, ..., P_4$	UNIK 5000	Draft tube	± 7 kPa (gauge)	$\pm 0.2\%$
P_5, P_6	Druck PDCR 810	Draft tube	7 kPa (gauge)	$\pm 0.1\%$
P_{vs}	UNIK 5000	Vaneless space	± 35 kPa (differential)	$\pm 0.04\%$
Q	Krohne Optiflux 2100	Waterway	± 12 m/s	$\pm 0.3\%$
ΔP	Honeywell FP2000	Turbine unit	± 50 kPa (differential)	$\pm 0.25\%$
T	HBM T22	Turbine shaft	± 0.5 N m	$\pm 0.5\%$
n	Omron Transmissive Photomicrosensor EE-SX461-P11	Turbine shaft	3 kHz	

where T and ω are the mechanical torque and runner angular frequency, respectively. Table 1 represents a list of the sensors used, along with their range and accuracy.

A National Instrument (NI) 9049 CompactRIO controller was used to collect the signals converted through analog-to-digital converter (ADC) cards. Two NI 9215 cards were used to record the time-resolved pressure signals, while the other signals were recorded using an NI 9205 ADC card. The cRIO was also used to operate the turbine and control the linear motors based on a program developed in LabVIEW. Table 2 displays the names and characteristics of the cards used on the cRIO with their function.

The physical diagram for the operation and control of the test rig and protrusion system is presented in Fig. 3. The cRIO receives the sensor signals from the connected ADC cards. The data is saved when measurements are taken, while the readings are continuously fed to the PLC subsystem during the turbine operation. The PLC actively compares the mean flow parameters from the cRIO data to those corresponding to the demanded operating point (OP). Thus, the required commands are transferred to the flow regulation tools, and the flow conditions are adjusted through the frequency of the pump, engagement of the magnetic brake, and control of the guide vane opening (GVO). Moreover, the cRIO feeds the position commands to the linear actuators using the NI 9264 cards to move the rods.

For the RVR mitigation measurements, four OPs were selected, which will be described in the upcoming sections. Under each OP, 11 protrusion lengths were investigated. For each case, after the stabilization of the mean flow parameters, the signals were recorded for 60 s. The experiments were organized in a GVO and protrusion length increasing

Table 2
Description of the ADC and DAC cards used for the data acquisition and test rig operation.

Module name	Function	Range	Resolution	accuracy
NI 9215	Analog input	± 10 V	16-bit	0.02%
NI 9205	Analog input	± 10 V	16-bit	0.03%
NI 9264	Analog output	± 10 V	16-bit	0.05%
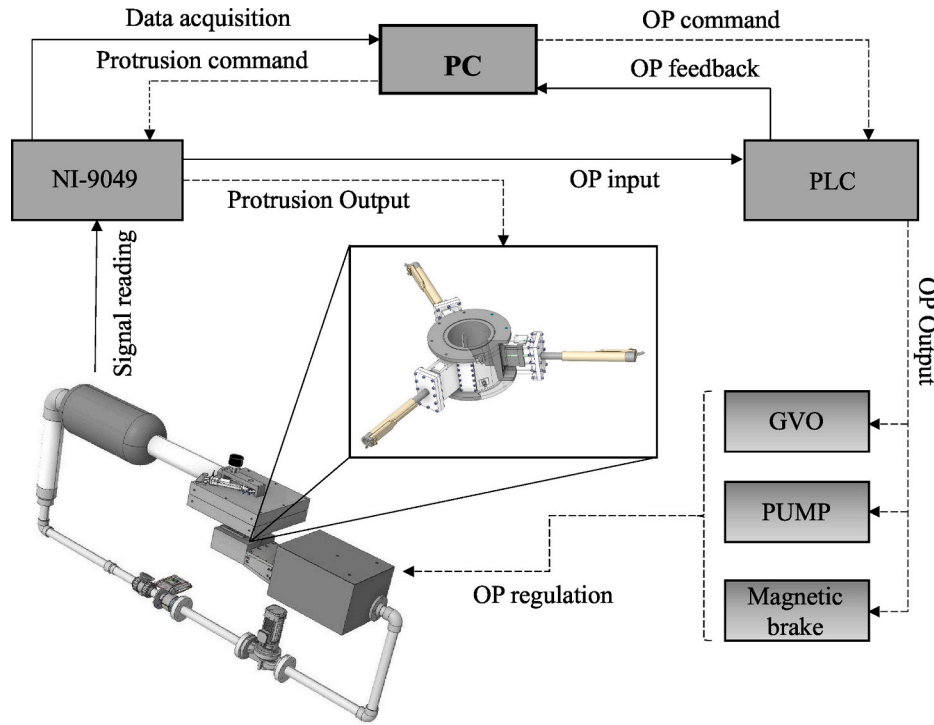
Fig. 3. Physical diagram for the operation of the test rig and the protrusion system. The blocks indicate the hardware involved. The solid and dashed arrows represent the reading input and command output, respectively.

order. Henceforth, the investigated protrusion lengths were first increased at a constant GVO angle corresponding to OP1. Once the OP1 measurements were performed for all the protrusion lengths of interest, the GVO was increased to higher OPs, and the increasing sweep of protrusion length was repeated. The data acquisition was performed at a frequency of 1 kHz, and each sweeping measurement was repeated at least three times, with the test rig being stopped between the repetitions.

3. Data analysis

3.1. Global flow parameters and repeatability

The global flow parameters presented for the investigated operating conditions and their respective repetitions were averaged as follows:

$$\overline{X} = \frac{\sum_{i=1}^{k} X_i}{k} \tag{3}$$

where k is the number of samples or repetitions, X_i is the value of the sample or repetition i. The standard deviations for both the averaged values as well as instantaneous data of different repetitions were calculated as follows:

$$\sigma = \sqrt{\frac{\sum_{i=1}^{k}(X_i - \overline{X})^2}{k-1}} \tag{4}$$

3.2. Time-resolved pressure data

The raw pressure signals were subtracted by their time-averaged value to obtain the fluctuating part as follows:

$$\widehat{P}_i(t) = P_i(t) - \overline{P}_i \tag{5}$$

where $P_i(t)$ is the instantaneous raw pressure recorded with the i-th sensor, and $\overline{P}_i$ is the time-averaged pressure amplitude of the same sensor. Aside from the analyses of $\widehat{P}_i(t)$, the signals were also decomposed into plunging and rotating modes, respectively, as follows [43]:

$$P_p(t) = \frac{1}{M} \sum_{i=1}^{M} \widehat{P}_i(t) \tag{6}$$

$$P_{r,i}(t) = \widehat{P}_i(t) - P_p(t) \tag{7}$$

where M is the number of sensors in each section. $P_p(t)$ and $P_{r,i}(t)$ are the plunging mode at the section of interest and the rotating mode at the location of the sensor P_i. Discrete Fourier transform (DFT) was performed on both the non-decomposed and decomposed signals to study the spectral content of the pressure signals. All the time-resolved pressure amplitudes and frequencies presented in this study are normalized based on the net head and runner frequency (n), respectively:

$$P^* = \frac{P}{\rho g H} \tag{8}$$

$$f^* = \frac{f}{n} \tag{9}$$

3.2.1. Statistical analyses of the RVR periodic characteristics

To investigate the periodic behavior of the RVR from the pressure data, a method proposed by Shiraghaee et al. [44] was used. This method is graphically demonstrated in Fig. 4. The fluctuating part of pressure signals (Fig. 4a) was first band-pass filtered at a range of about $\pm 0.15n$ around the RVR frequency, and the peak values were determined, as shown by the star symbols in Fig. 4b. The data between each two consecutive peaks corresponds to those of one vortex rope rotation. The duration between two consecutive peaks indicates the period of a single vortex rope precession. The difference between the maximum and minimum amplitude in each period is designated as the period's peak-to-peak (P2P) amplitude. Then, the P2P and the corresponding frequencies for each period are extracted, as illustrated in Fig. 4c and d, respectively. Each P2P point is then mapped against their respective frequencies (Fig. 4e). The resulting map can be obtained for the RVR under the different protrusion lengths. Thus, the impact of the protrusion can be studied on the RVR periodicity through a comparison of how
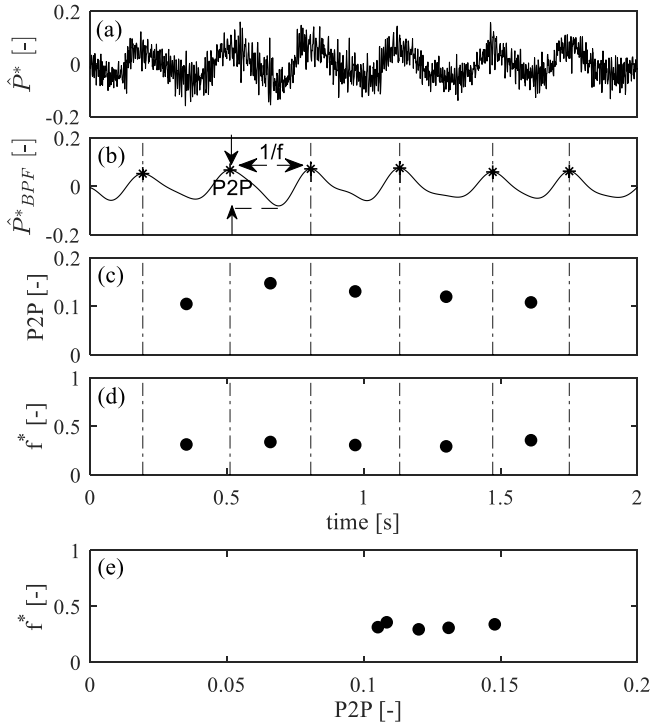
Fig. 4. An illustration of how the P2P vs. f map is produced. a) Raw pressure signal fluctuating part. b) Signal filtering around the RVR frequency. c) Determining the P2P amplitudes for each RVR period (indicated between the dashed dotted lines). d) Determining the RVR frequency for each period. e) Creating the distribution with each point representing the RVR frequency and its respective P2P.

scattered the distributions become after the protrusion.

3.2.2. Pressure data phase-averaging

To study the phase-averaged data from each pressure sensor with respect to the others, the pressure data of the first pressure sensor at each section were first filtered around the RVR frequency, similar to section 3.2.1. These sensors were P_1 at section A, and P_4 at section B. Fig. 5 schematically displays the phase-averaging process of the filtered pressure data. After filtering the pressure data, the peaks were extracted as the beginning point of each period, as indicated by the star symbol in Fig. 5a. The time-resolved data points between every two consecutive peaks -that correspond to an RVR rotation period- were rearranged into a single window. Each window starts at a phase of $\varphi = 0°$ and ends at $\varphi = 360°$, as presented in Fig. 5b. Next, the phase-resolved data were divided into equal bins with a size of $\Delta\varphi = \theta = 1°$, as schematically represented by the vertical dotted lines in Fig. 5b. Each bin in the time-series data (vertical dotted lines in Fig. 5a) contains the RVR pressure amplitude between $\varphi = \varphi_0$ and $\varphi = \varphi_0 + \theta$. Thus, the data of the different periods that are within the same bin represent the RVR-induced pressure amplitudes at a particular phase for the different periods (vertical dotted lines in Fig. 5b). Then, the data points within each bin were averaged to extract the phase-averaged pressure data for the sensor, as indicated by the red dashed line in Fig. 5b.

After extracting the phase-averaged pressure data for the first sensor on a section, the points of consecutive peaks -that were used for the RVR identification- on the first sensor were used to define the RVR periods on the neighboring sensor. Consequently, when the RVR was captured inducing the peak pressure amplitude on the first sensor, the RVR amplitude could be identified simultaneously on the neighboring sensor. The points corresponding to these instances are indicated for the second sensor by the star symbol in Fig. 5c. Then, the data of the second sensor were rearranged and divided into bins, as explained above, and the phase-averaged data were extracted with respect to the first sensor. This
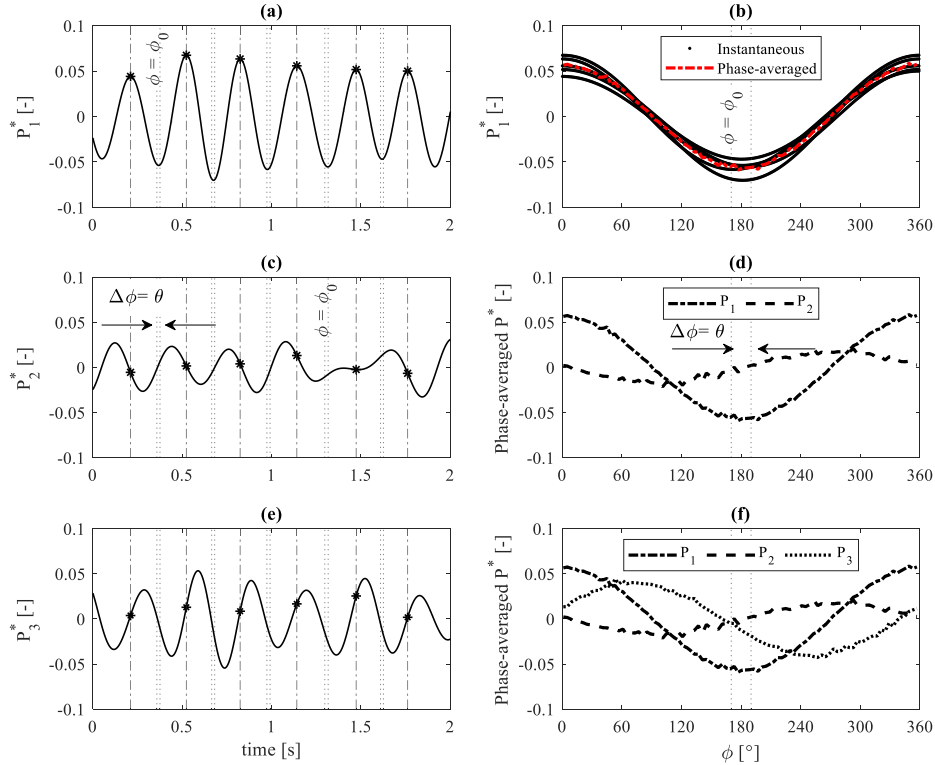
Fig. 5. An illustration of the pressure data phase-averaging. a) Determining the RVR periods in the RVR-filtered pressure data. b) Superposing the determined periods and averaging within the defined phase windows (bins). c) Using the defined periods and bins in (a) for the second sensor. d) Phase-averaging the signals from the second sensor based on the defined periods in (a). e) Using the defined periods in (a) for the third sensor. f) Phase-averaging the signals from the third sensor relative to the first sensor.

step is graphically displayed in Fig. 5d. Finally, the same procedure was repeated for the third sensor in the same plane (Fig. 5e and f).

3.2.3. Vortex rope coherence

Magnitude-squared coherence (MSC) function was applied to the recorded pressure data from section A to study the coherence of the vortex structure in the draft tube. The coherence values in this method are calculated based on the spectral content of two signals separated in phase to exhibit a measure of the signals' linearity in the frequency domain [45]. Varying between one and zero, the MSC is expressed as follows:

$$C_{xy} = \frac{|G_{xy}|^2}{G_x G_y} \tag{10}$$

where G_{xy} is the cross-power spectral density of the signals x and y estimated using Welch's method, and G_x and G_y denote the estimated power-spectral densities for x and y, respectively [46]. In this study, the signals P_1 and P_2, which are divided by 120° at section A, were selected to obtain the MSC of the vortex structure. Fig. 6 demonstrates the spectra for the power-spectral density of P_1 (G_{P_1}), and the corresponding MSC estimation using P_1 and P_2 ($C_{P_1P_2}$) under a PL condition with the presence of the RVR. The G_{P_1} peaks observed for $f^* < 1$ display low coherences with the exception of two peaks at $f^* \simeq 0.3$ and $f^* \simeq 0.6$ where the MSC values exceed 0.9. These two coherent structures appearing in the draft tube under the PL are attributed to the RVR fundamental mode and its harmonic.

Under the investigated operating conditions, the $C_{P_1P_2}$ values were obtained for the dominant frequency in the P_1 Fourier spectra. Thus, the coherence of the vortex structure could be compared alongside its spectral magnitude under each condition.

4. Results

4.1. Operating point selection

To select OPs that are representative of the full turbine PL range, a hill chart of the turbine was prepared based on PL measurements performed under 56 operating conditions away from the BEP. Fig. 7 shows the model turbine hill chart in the PL range. The efficiency values are normalized with that of the BEP (η/η_{BEP}). Also, the amplitude of the dominant peak in the low-frequency region ($f^* < 1$) was extracted from the P_1 Fourier spectra under each operating condition. These values, represented by dotted dashed contours, are superposed on the turbine hill chart, allowing a comparison of the amplitude of RVR-induced
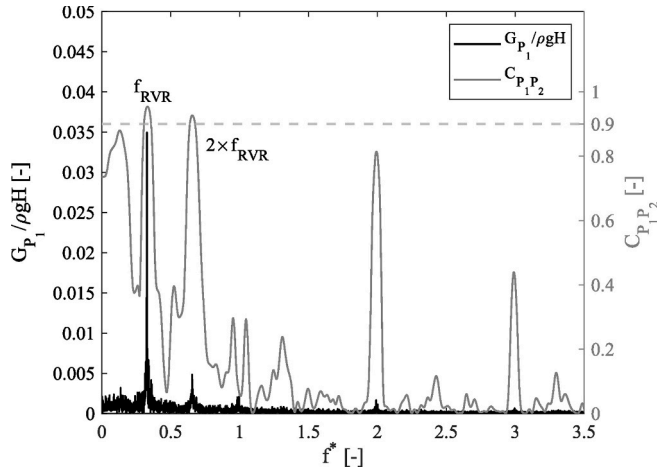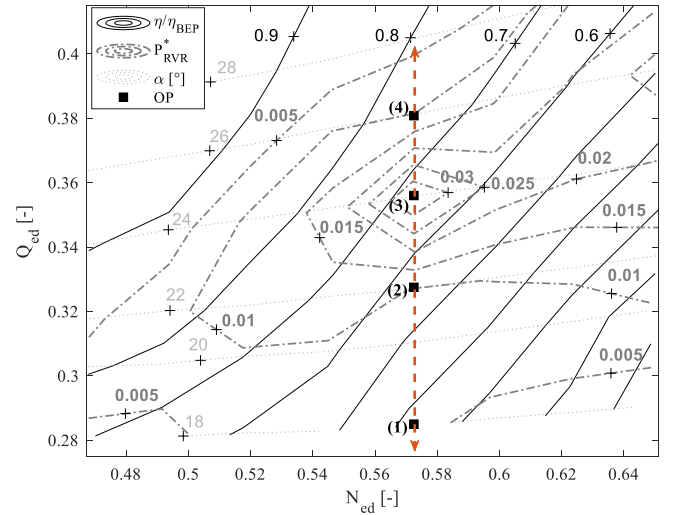

Fig. 7. Turbine hill chart at PL and the corresponding RVR P_{RVR}^* amplitudes. The red dashed arrow indicates the propeller curve, and the solid squares represent the OPs selected for the RVR mitigation.

pressure oscillations (P_{RVR}^*) between the studied PLs. The P_{RVR}^* values are normalized by the turbine net head.

A series of concentric P_{RVR}^* zones are observed between $\eta/\eta_{BEP} = 0.5$ to $\eta/\eta_{BEP} = 0.8$ with the highest RVR-related amplitude occurring at $N_{ed} = 0.57$ and $\alpha = 24°$. To investigate the evolution of the RVR-induced pressure pulsations, a propeller curve was defined around this point with the most robust oscillations. In other words, different GVOs corresponding to different values of Q_{ed} were further investigated at a constant speed factor of $N_{ed} = 0.57$, thus replicating conditions ranging from deep to upper part load. The selected propeller curve is indicated with the red dotted dashed arrow in Fig. 7.

Fig. 8 displays the spectral amplitude of the dominant low-frequency pressure oscillations and their respective MSC values over the selected propeller curve.

The spectral amplitude for the dominant frequency of pressure pulsations is 0.6% of the net head at $\alpha = 18°$ with a relatively low coherence of $C_{RVR} = 0.83$. As the GVO increases, the spectral amplitude of the vortex structure gradually increases along with its coherence until $\alpha = 22°$, where the coherence exceeds 90% with an amplitude of $P_{RVR}^* = 0.009$. For $\alpha = 24°$, P_{RVR}^* and the MSC reach their maximum values of 0.035 and 0.96, respectively. The RVR loses coherence with the increase of the guide vane opening angle, and its amplitude of induced pressure
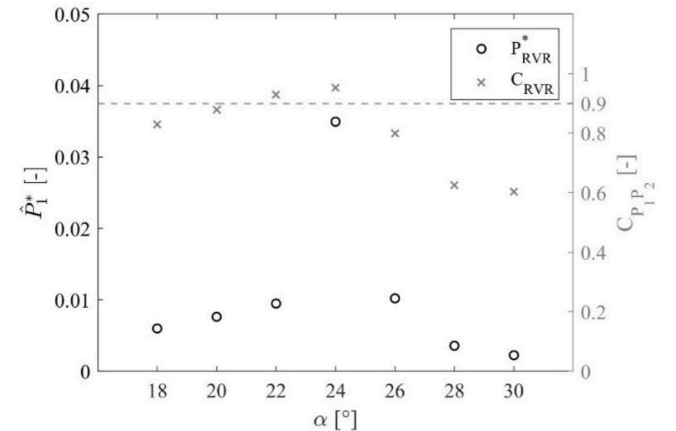

Fig. 6. Power spectral density of the P_1 recorded signals at PL and the corresponding MSC spectra obtained P_1 and P_2.

Fig. 8. The spectral amplitude of the dominant low-frequency pressure oscillations and their corresponding MSC values for the OPs comprising the selected propeller curve.

pulsations decreases. The vortex rope becomes considerably noncoherent after, with the MSC values dropping below 0.8, which shows the decay of the RVR at upper PL operation.

Four points were chosen from the discussed propeller curve to perform RVR mitigation with flat-plate protrusion. These operating points are denoted as OP1, OP2, OP3, and OP4 corresponding to GVOs of $\alpha = 18°, 22°, 24°$, and $26°$. These points represent the RVR-induced pressure pulsations over the turbine's PL range. Table 3 displays the global flow parameters corresponding to each OP.

4.2. Test rig repeatability

In this section, the repeatability of the test rig is analyzed under the investigated operating points. To this end, a repeatability assessment of the fixed global flow parameters (n and H), and of the pressure oscillations in the range specific to each operating point is examined. This way, the test rig repeatability in providing the conditions specific to each OP could be quantified.

As forementioned, under all conditions of the perturbed and unperturbed flow, the head (H) and runner rotational frequency (n) were attempted to be kept constant at H = 0.3 m and n = 10 Hz, respectively. Fig. 9 shows the probability distribution and density function for the obtained H and n based on five cases randomly selected from all the investigated operating conditions and protrusion lengths. The recorded resulting distributions display standard deviations of 0.38% and 1.35% of the mean values for the parameters n (σ_n) and H (σ_H), respectively.

To investigate the reproducibility of the flow pressure oscillations for each operating point, five repetitions were studied for one sensor in the draft tube. Hence, the histograms of probability density were drawn based on each of the five repetitions for the unperturbed cases of the different operating points. Then, a probability density function (PDF) line was fitted to each histogram, and the PDF lines for the different repetitions were drawn and compared against one another to see how well the different fits collapsed on one another. For this purpose, the range between the minimum and maximum amplitude under each operating point was divided into 100 bins, and the average probability and standard error (S.E) in each bin were calculated for the five repetitions according to S.E $= \sigma/\sqrt{5}$.

Fig. 10 shows the PDF of $\widehat{P}_1^*$ for five repetitions of pressure measurements under each operating point without any plate protrusion. The red lines indicate the bin-averaged values, while the dotted line demonstrates the standard error of probability at the given pressure amplitudes. The 95% confidence intervals are marked with the dotted dashed lines. The range of the oscillation amplitudes decreases from OP1 to OP4. The flow conditions in the draft tube shift from those similar to speed-no-load at OP1 (Fig. 10a) to the upper part load in the proximity of the BEP at OP4 (Fig. 10d). Consequently, the swirl in the draft tube decreases from OP1 to OP4, which results in the decrease of the swirl-induced flow instabilities as implied by the amplitude of the pressure oscillations. The S.E increases near the tails of the distributions for all figures due to the small probability of the large amplitude oscillations. Finally, the uncertainties -implied by the S.E− are below 5% in the amplitude ranges corresponding to the RVR and low-frequency oscillations in the draft tube, as will be discussed in the upcoming section. So, the figures in the results section can be examined with regard to the S.E levels specified in Fig. 10.

Table 3
Global flow parameters of the operating conditions selected for flat-plate protrusion.

Operating condition		OP1	OP2	OP3	OP4
Guide vane angle	α (°)	18	22	24	26
Flowrate	Q (l/s)	4.51	5.23	5.73	6.18
Speed factor	n_{ed} (−)	0.57	0.57	0.57	0.57
Discharge factor	Q_{ed} (−)	0.28	0.32	0.35	0.38

4.3. Effect of the flat plates on the pressure pulsations

The results of flat-plate protrusion are discussed in this section. The protrusion lengths presented are normalized based on the draft tube radius at the bottom of the plates ($L^* = L/R_{DT}$).

4.3.1. Spectral analyses

Fig. 11 displays Fourier spectra of the rotating mode for the sensor P_1 ($P_{r,1}$) and plunging mode at section A ($P_{p,A}$) for the different protrusion lengths under each operating point.

The dominant source of the oscillations lies within the low-frequency range ($f^* \leq 1$) for all operating points. When the flow is unperturbed ($L^* = 0$), the dominant peak at low frequency becomes sharper from OP1 (Fig. 11a) to OP4 (Fig. 11d). Also, the wide-band-frequency oscillations decrease from OP1 to OP4, which determines the formation of a uniform RVR and the decrease of non-periodic oscillations. The rotating mode of the unperturbed RVR increases from OP1 to OP3 regardless of the swirl decrease that occurs from deep to upper PL. This occurs due to the development of a periodic behavior and increased RVR coherence, as discussed earlier. The plunging mode becomes stronger from OP1 to OP3 and is almost equal to the rotating mode at the upper part-load conditions present at OP4.

The protrusion of the plates causes a gradual decrease in the amplitude of the dominant frequencies under all conditions. For the cases where the peak corresponding to the RVR stands out close to $f^* = 0.3$ (Fig. 11b, c, d), the RVR frequency increases with L^*. The RVR peak and its harmonic completely disappear at $L^* = 0.67$ for OP2, OP3, and OP4 in Fig. 11b, c, and d, respectively. However, a single scattered peak reappears at $L^* = 0.83$ for OP2 and OP3, close to $f^* = 0.6$ (Fig. 11b and c).

PL pressure oscillations originate from the draft tube as a result of the RVR formation [16]. They can damage the turbine moving parts, both due to the proximity of the local oscillations (rotating mode) to the rotor and the occurrence of resonance due to the axial perturbations (plunging mode) traveling upstream [39]. Given the dominant contribution of the rotating mode to the overall magnitude of pressure oscillations in the draft tube and the swirling flow's essential role in the RVR inception, it is critical to address the swirl in mitigating the RVR. In addition, an effective mitigation method in the draft tube should be able to dampen the oscillations not just locally but also upstream of the draft tube where the rotor is located. Hence, it is essential to investigate if the same mitigation trends are obtained upstream of the draft tube as well. Fig. 12 displays the Fourier spectra of the pressure sensor installed in the vaneless space (P_{vs}) for different L^* under the different operating points.

The pressure amplitude of the peak corresponding to the unperturbed RVR (Fig. 12b, c, d) under each operating point is similar to that of the plunging mode in Fig. 11. The plunging mode of the RVR-induced pressure oscillations has been addressed in the literature as a global phenomenon that travels upstream and downstream in the entire conduit [16]. Therefore, its amplitude does not vary significantly at different axial levels [44]. Ultimately, under the PL conditions investigated, the origin of the pressure oscillations lies in the draft tube. So, it is only the global mode of the oscillations that reaches the vaneless space.

Moreover, the trends for the RVR mitigation are similar in the vaneless space (Fig. 12) to those observed in the draft tube shown in Fig. 11. Thus, the RVR-induced oscillations are successfully stopped from traveling upstream, and the mitigation method is effective globally and not just close to the diffuser wall where the draft tube pressure sensors are located. For OP1, however, the oscillations are spread in a wide-band frequency range, and no clear peak stands out, indicating the stochastic behavior of the vortical flow under this condition.

4.3.2. Mechanism

So far, the overall impact of the mitigation method on the pressure oscillations has been discussed based on spectral analyses. It was observed that the oscillations decreased with the plate protrusion. The
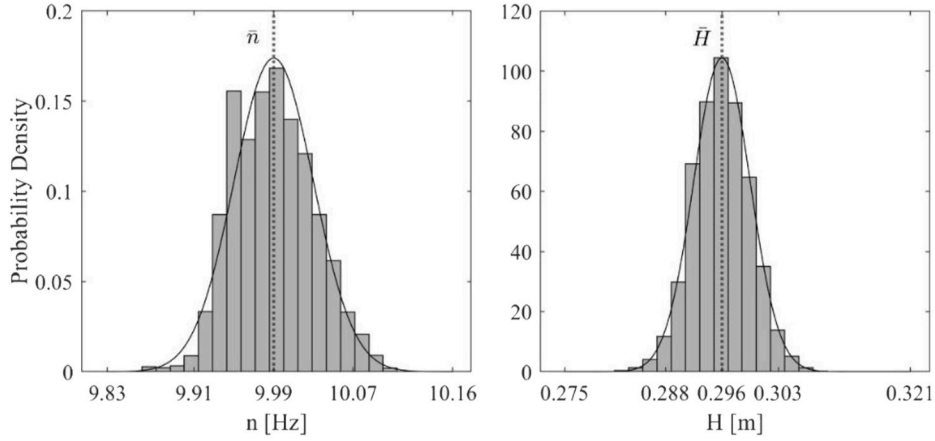
Fig. 9. Probability distribution and corresponding probability density function of *n* (left) and *H* (right) for five repetitions.
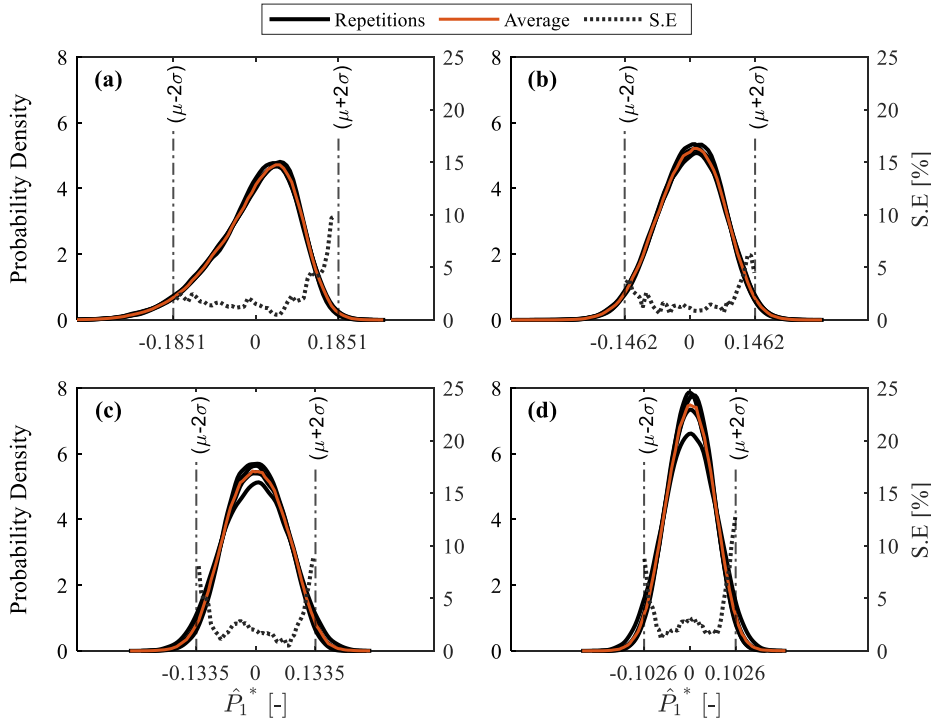

Fig. 10. Probability density function of the pressure oscillations for five repetitions under the different operating conditions. a) OP1, b) OP2, c) OP3, d) OP4.

phase-averaged pressure signals can determine the change in the RVR structure caused by its interactions with the plates. To understand the underlying mitigation mechanisms, the RVR under OP3 is investigated in this section since it induces the strongest pressure oscillations.

Fig. 13 shows the phase-averaged pressure of the different sensors at sections A and B for the unperturbed and mitigated RVR under OP3.

In the absence of the plates, the signals from the sensors have significant and unequal phase differences at section A. It was demonstrated in a previous study that as the vortex rope passes near a pressure sensor in the draft tube, the low-pressure vortex induces a valley in the sinusoidal RVR-related pressure data; thus, large phase differences between the sensors around the draft tube indicate a wider path of the RVR [44]. The phase difference between the signals from P_3 and P_1 is $\varphi_1 - \varphi_3 = 98°$ while $\varphi_2 - \varphi_1 = 83°$, as shown in Fig. 13a. These observations, along with a difference of 150% between the maximum and minimum unperturbed amplitudes at section A, pertain to the eccentricity and asymmetry of the RVR precession. The same behavior can be observed for the unperturbed RVR at section B, shown in Fig. 13b. The protrusion

of the plates is speculated to cause a restriction of the vortex core in the draft tube center reducing its asymmetry.

For a plate protrusion of $L^* = 0.83$, the plates almost meet at the draft tube center, and the swirl entering the draft tube is directed and focused between the plates. The negligible phase differences in Fig. 13c imply that only minor oscillations occur in the plunging mode with a protrusion of $L^* = 0.83$. Thus, the vortex-induced oscillations are almost completely mitigated at section A. Flow visualizations in the investigation of rod protrusion on a larger model scale of the U9 turbine showed that the vortex path is restricted when the phase differences between the draft tube sensors are minimal [42]. The imposed flow conditions under $L^* = 0.83$ do not allow a wide precession of the RVR, and the small phase and amplitude differences at section A demonstrate the restriction of the vortex path. At section B, the phase differences increase again between the sensors, as shown in Fig. 13d. The signals from P_4 are in opposite phase compared to those of P_6, while their amplitude ranges are quite similar. On the other hand, the sensor P_5 displays an almost flat phase-averaged pressure oscillation. This shows that the vortex
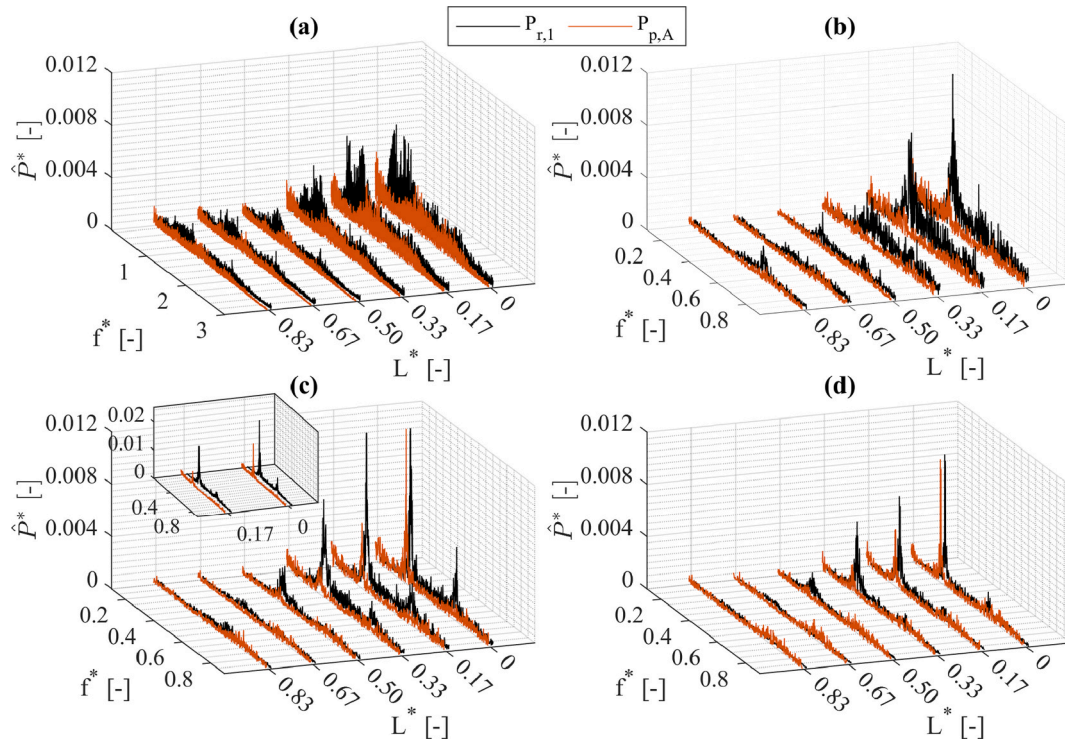
Fig. 11. Fourier spectra of the decomposed pressure signals at section A for the different operating points and protrusion lengths. a) OP1, b) OP2, c) OP3, d) OP4. The spectra for $L^* = 0$ and $L^* = 0.17$ are cropped under OP3 to demonstrate the smaller peaks better. The small subplot, therefore, represents the complete peaks for $L^* = 0$ and $L^* = 0.17$.
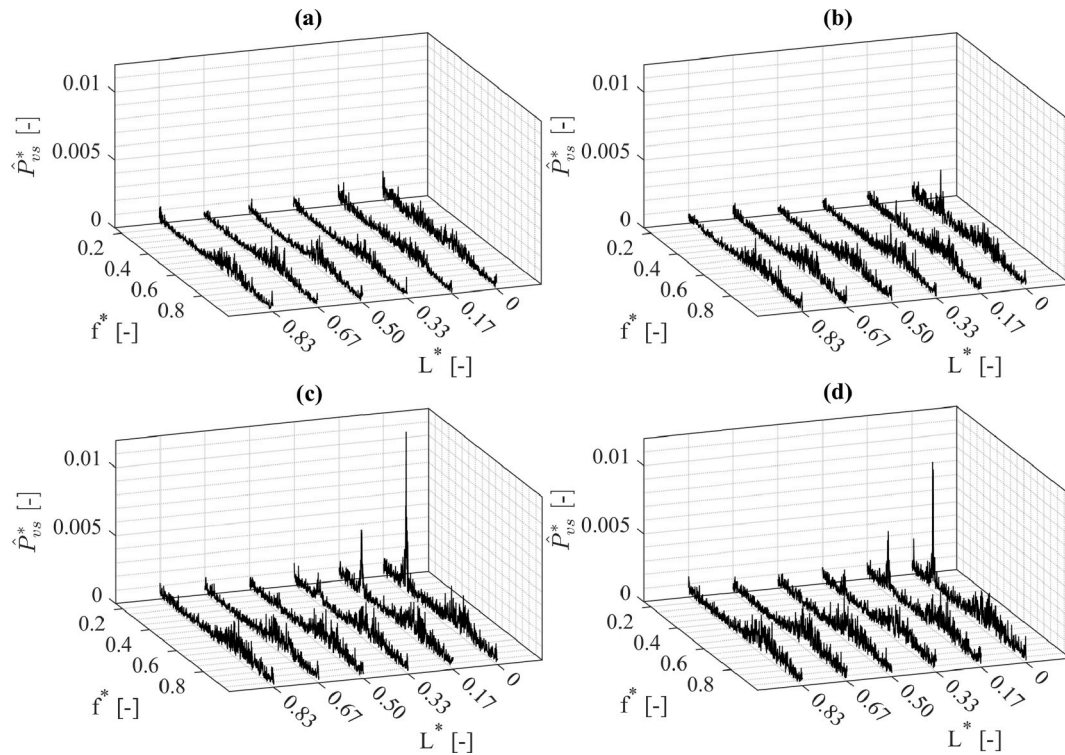
Fig. 12. Fourier spectra of the pressure signals recorded in the vaneless space for the different operating points and protrusion lengths. a) OP1, b) OP2, c) OP3, d) OP4.

precession takes place in an oval path under the flat plates with the longer diagonal axis directed at P_4 and P_6. Also, the small amplitude at P_5 as well as the similar amplitudes at P_4 and P_6 indicate that the oval

path of the vortex is bent towards the elbow bend. Overall, the amplitudes are significantly smaller at section B compared to the unperturbed state, which implies a significant mitigation even at the downstream
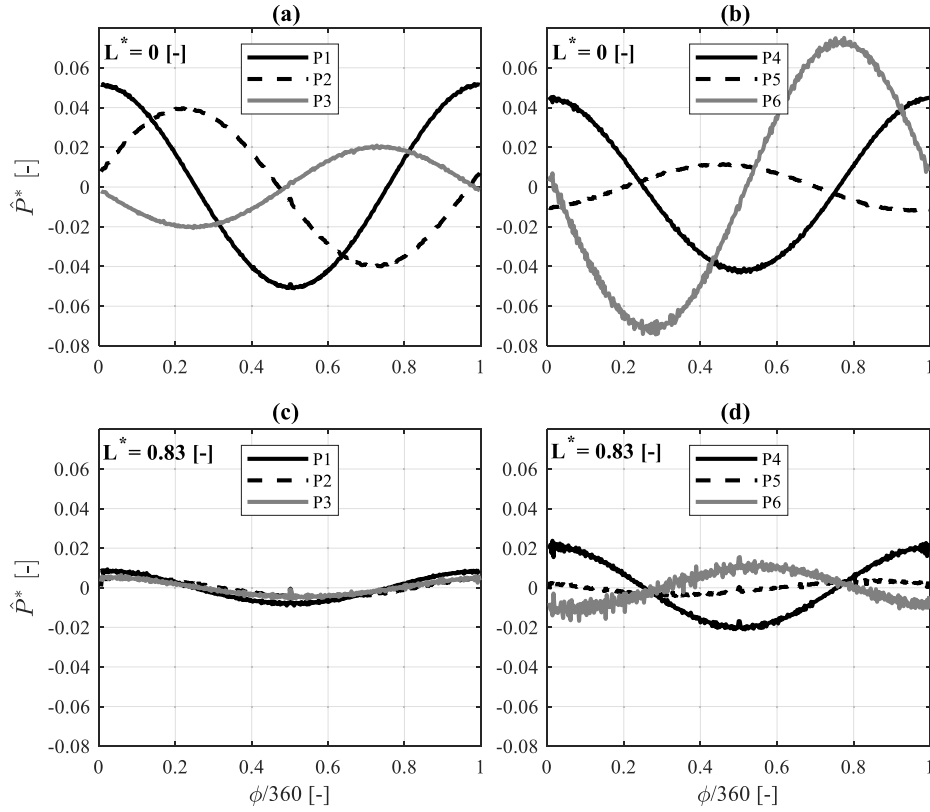
Fig. 13. Phase-averaged pressure of the sensors at sections A and B for OP3 under different protrusion lengths.

level.

Next, the impact of the mitigation method is studied on the periodicity and coherence of the RVR-induced oscillations. The latter is done through statistical analysis of the periodic P2P amplitudes and frequencies explained in section 3.2.1. Also, the MSC amplitudes for the dominant frequency of pressure oscillations are displayed for each protrusion length. Fig. 14 shows the peak-to-peak vs. frequency distribution of $\widehat{P}_1^*$ for the unperturbed and mitigated RVR under OP3 at
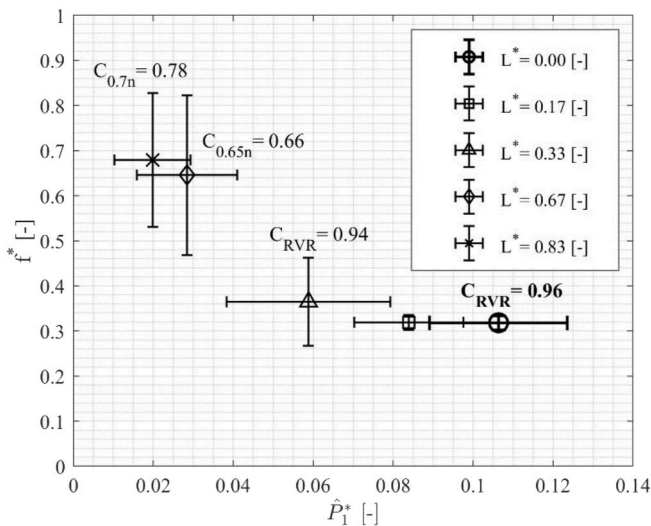

Fig. 14. Peak-to-peak vs. frequency distribution of $\widehat{P}_1^*$ at section A for the different protrusion lengths under OP3. C indicates the MSC value for the dominant frequency of pressure oscillations under the respective protrusion lengths. The subscript on C shows the dominant frequency of pressure oscillations.

section A. The markers indicate the average value, and the error bars show one standard deviation.

The unperturbed RVR has a high periodicity, meaning that the variations in its frequency are insignificant. The frequency distribution becomes more dispersed with protrusion, i.e., the RVR frequency variations increase. In addition, the average RVR frequency increases, too, with the protrusion of the plates. The average vortex rope frequency almost doubles at $L^* = 0.83$ compared to $L^* = 0$. A similar pattern has been observed by Shiraghaee et al. [39] when RVR mitigation was realized using circular rods instead of flat plates. The protrusion of the plates constricts the area available for the swirling flow passage, causing a stretch of the vortex. Thus, the swirling frequency should increase for the angular momentum to be conserved [47]. With the increase of protrusion length, the RVR frequency dispersion further increases, and the vortex coherence is significantly affected after $L^* = 0.33$. At this point, the vortex structure changes to a constricted and straight vortex, as argued in the discussion relating to Fig. 13c. The frequency dispersion of the vortex rope decreases by 17% from $L^* = 0.67$ to $L^* = 0.83$, while the coherence increases by 12%. This shows that the shifted structure stabilizes with an increased protrusion, which explains the reappearance of a single scattered peak in Fig. 11c. However, it is not just the manipulated periodicity of the vortex structure that leads to the significant spectral mitigation in Fig. 11. Fig. 14 clearly shows that the RVR-induced amplitude of the oscillations reduces by approximately 85%. Thus, the RVR is successfully mitigated upstream of the plates.

4.4. Effect of the flat plates on efficiency

The turbine efficiency was calculated using Eq. (2). Since the parameters ω and H are constant in the experiments, only the torque (T) and flowrate (Q) contribute to the changes in the efficiency as a result of flat-plate protrusion. Moreover, T predominantly consists of the hydraulic torque (T_h) that is correlated with Q in hydraulic machinery according to Euler's turbine equation as follows [48]:

$$T_h = \frac{\rho Q}{2\pi}(\Gamma_1 - \Gamma_2) \tag{11}$$

where Γ_1 and Γ_2 denote the mean circulation in the flow entering and leaving the runner blades, respectively. The swirl is generated by the guide vanes; therefore, at a constant guide vane opening angle (corresponding to one operating condition), Γ_1 depends linearly on Q, and the torque is subsequently roughly correlated with the flowrate as:

$$\Gamma_1 \sim Q \rightarrow T \sim Q^2 \tag{12}$$

Thus, T is normalized with Q^2 ($T^* = T/Q^2$), and the resulting parameter is then correlated with Γ_2 as shown below:

$$T^* \sim 1 - \frac{\Gamma_2}{Q} \sim 1 - \frac{\Gamma_2}{\Gamma_1} \tag{13}$$

Thus, a comparison of the T^* values for the different protrusion lengths under the same operating point (minor Γ_1 changes) can help study the impact of the flow circulation leaving the runner (Γ_2) on the efficiency. Fig. 15 represents the relative changes in the turbine efficiency (η) and normalized torque (T^*) against L^* under each operating condition. η_{L0} and T_{L0}^* denote the efficiency and normalized torque measured for the unperturbed flow, respectively.

The trends for the efficiency follow those of torque for each operating point. Under OP1 and OP2, the efficiency starts increasing with the protrusion of the plates and then gradually decreases from the maximum level (Fig. 15a and b). Under OP3 and OP4, however, the changes are insignificant at shorter protrusion lengths. At the same time, some decrease in the efficiency can be observed for higher values of L^* compared to the unperturbed state. The residual swirl that enters the draft tube under PL operations causes a decrease in the efficiency [8]. Thus, the reduction of vortex orbit (as seen in Fig. 13c) to the draft tube center demonstrates constriction of the stagnant zone. This leads to a modified performance of the draft tube, causing an increase in efficiency. The efficiency increase is significantly more pronounced under the lower PL conditions (OP1 and OP2) compared to the upper PL (OP3 and OP4) since the stagnant zone is wider under the former conditions.

The presence of flat plates under these conditions increases T^*, which implies that the negative term in Eq. (13) decreases. Thus, the decrease in the circulation at the runner outlet (Γ_2) as a result of flat-plate protrusion causes an increased torque, which, in turn, leads to an increase in the efficiency. Nevertheless, longer protrusions lead to a decrease in the efficiency, possibly due to the increased losses. Finally, the efficiency under lower PL operations is low as shown in Fig. 7 due to the low flowrates and corresponding torques. Therefore, slight changes in the torque result in significant relative variations in the normalized torque and efficiency. This explains the large error bars as well as increments in Fig. 15a.

5. Conclusion

A novel concept of flat-plate protrusion was investigated on a scaled-down propeller turbine to mitigate the RVR-induced pressure oscillations at PL operating conditions. The mitigation system consisted of three flat plates that could be inserted into the draft tube at variable protrusion lengths. Pressure and efficiency measurements were performed under four operating points to quantify the RVR mitigation and its impact on turbine efficiency. The main conclusions drawn from the experiments can be listed as follows:

a) The proposed method can successfully dampen -and for certain operating points completely suppress- the RVR-induced pressure oscillations both in the draft tube and upstream of the runner.
b) The mitigation inhibits the flow circulation in the draft tube wall proximity, hence restricting and straightening the vortex core in the draft tube center.
c) An increase in the protrusion length reduces the flow asymmetry in the draft tube.
d) Under lower PL operating conditions, the proposed method initially increases the hydraulic efficiency of the system. This effect is due to an increase in the hydraulic torque, which is attributable to the vortical flow being constricted and directed to the draft tube center, modifying the draft tube's performance. Past a certain level of
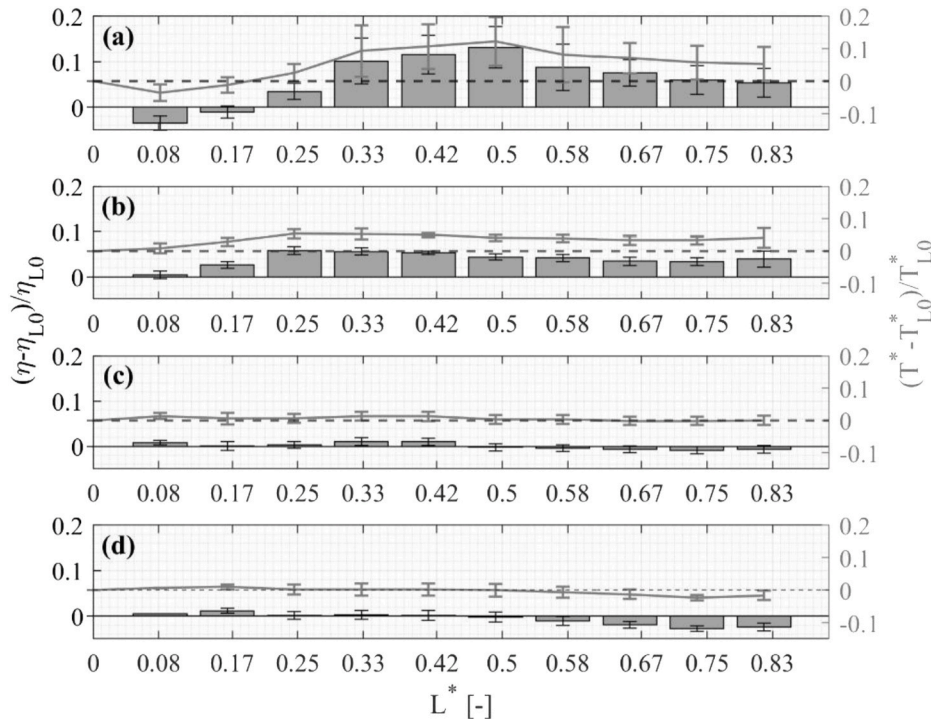

Fig. 15. Changes in the efficiency and normalized torque against protrusion length for the different operating points. a) OP1, b) OP2, c) OP3, d) OP4. The bars and lines indicate the normalized efficiencies and normalized torque, respectively.

maximum efficiency, further protrusion presumably introduces additional losses, which lowers the efficiency for those operating conditions.

e) The impact on the efficiency is more pronounced under lower PL conditions where the swirl is stronger.

The proposed technique appears promising towards a complete mitigation of the PL pressure oscillations. Given the adjustment flexibility of the system, it is beneficial to couple it with a feedback-loop controller to regulate the length of protrusion concurrently based on a suitably selected objective function.

CRediT authorship contribution statement

Shahab Shiraghaee: Formal analysis, Investigation, Writing – original draft. **Joel Sundström:** Formal analysis, Methodology, Writing – review & editing. **Mehrdad Raisee:** Formal analysis, Writing – review & editing. **Michel J. Cervantes:** Formal analysis, Supervision, Writing – review & editing.

Declaration of competing interest

The authors declare the following financial interests/personal relationships which may be considered as potential competing interests: Michel J. Cervantes reports financial support was provided by Horizon 2020 research and innovation program.

Acknowledgments

References

[1] Bhattarai, H., "Hydropower and Sustainability," Technological Innovations and Advances in Hydropower Engineering..

[2] Hydropower Status Report, 2022.

[3] A. Soltani Dehkharqani, F. Engström, J.-O. Aidanpää, M.J. Cervantes, Experimental investigation of a 10 MW prototype kaplan turbine during start-up operation, Energies 12 (23) (2019) 4582.

[4] R. Goyal, B.K. Gandhi, Review of hydrodynamics instabilities in Francis turbine during off-design and transient operations, Renew. Energy 116 (2018) 697–709.

[5] A. Favrel, J. Gomes Pereira Junior, C. Landry, A. Müller, C. Nicolet, F. Avellan, New insight in Francis turbine cavitation vortex rope: role of the runner outlet flow swirl number, J. Hydraul. Res. 56 (3) (2018) 367–379.

[6] H. Cheng, L. Zhou, Q. Liang, Z. Guan, D. Liu, Z. Wang, W. Kang, A method of evaluating the vortex rope strength in draft tube of Francis turbine, Renew. Energy 152 (2020) 770–780.

[7] N. Sotoudeh, S. Shiraghaee, R. Andersson, J. Sundstrom, M. Raisee, M. Cervantes, PIV Measurements in the Draft Tube of a Down-Scale Propeller Turbine: Uncertainty Analysis," *IOP Conference Series: Earth And Environmental Science*, IOP Publishing, 2022 012065.

[8] A. Muhirwa, W.-H. Cai, W.-T. Su, Q. Liu, M. Binama, B. Li, J. Wu, A review on remedial attempts to counteract the power generation compromise from draft tubes of hydropower plants, Renew. Energy 150 (2020) 743–764.

[9] Z. Seifi, M. Raisee, M.J. Cervantes, Global linear stability analysis of flow inside an axial swirl generator with a rotating vortex rope, J. Hydraul. Res. 61 (1) (2023) 34–50.

[10] H. Foroutan, S. Yavuzkurt, Unsteady numerical simulation of flow in draft tube of a hydroturbine operating under various conditions using a partially averaged Navier–Stokes model, J Fluids Eng 137 (6) (2015).

[11] S. Pasche, F. Gallaire, F. Avellan, Origin of the synchronous pressure fluctuations in the draft tube of Francis turbines operating at Part Load conditions, J. Fluid Struct. 86 (2019) 13–33.

[12] C. Nicolet, A. Zobeiri, P. Maruzewski, F. Avellan, Experimental investigations on upper Part Load vortex rope pressure fluctuations in Francis turbine draft tube, International Journal of Fluid Machinery and Systems 4 (1) (2011) 179–190.

[13] A. Favrel, Z. Liu, K. Miyagawa, Resonator-like behavior of a wall-bounded precessing vortex core in a diffuser with wall asymmetries, Phys. Fluids 35 (3) (2023).

[14] M. Nishi, T. Kubota, S. Matsunaga, Y. Senoo, Study on Swirl Flow and Surge in an Elbow Type Draft Tube, Proc. IAHR 10th Symp., Tokyo, Japan, 1980, pp. 557–568.

[15] R. Goyal, M.J. Cervantes, B.K. Gandhi, Vortex rope formation in a high head model Francis turbine, J Fluids Eng 139 (4) (2017).

[16] K. Amiri, B. Mulu, M. Raisee, M.J. Cervantes, Unsteady pressure measurements on the runner of a kaplan turbine during load acceptance and load rejection, J. Hydraul. Res. 54 (1) (2016) 56–73.

[17] P.P. Jonsson, B.G. Mulu, M.J. Cervantes, Experimental investigation of a kaplan draft tube–Part II: off-design conditions, Appl. Energy 94 (2012) 71–83.

[18] S. Kumar, M.J. Cervantes, B.K. Gandhi, Rotating vortex rope formation and mitigation in draft tube of hydro turbines–A review from experimental perspective, Renew. Sustain. Energy Rev. 136 (2021) 110354.

[19] R. Susan-Resiga, T.C. Vu, S. Muntean, G.D. Ciocan, B. Nennemann, Jet Control of the Draft Tube Vortex Rope in Francis Turbines at Partial Discharge," *23rd IAHR Symposium Conference*, 2006, pp. 67–80.

[20] A.I. Bosioc, R. Susan-Resiga, S. Muntean, C. Tanasa, Unsteady pressure analysis of a swirling flow with vortex rope and axial water injection in a discharge cone, J Fluids Eng 134 (8) (2012).

[21] H.J. Juposhti, R. Maddahian, M.J. Cervantes, Optimization of axial water injection to mitigate the rotating vortex rope in a Francis turbine, Renew. Energy 175 (2021) 214–231.

[22] A.I. Bosioc, C. Tănasă, Experimental study of swirling flow from conical diffusers using the water jet control method, Renew. Energy 152 (2020) 385–398.

[23] I.K. Vilberg, M. Kjeldsen, X. Escaler, J.V. Ekanger, T.K. Nielsen, Influence of draft tube water injection system on cavitation behaviour in a full-scale Francis turbine with visual access. IOP Conference Series: Earth and Environmental Science, IOP Publishing, 2019 022015.

[24] B. Papillon, M. Sabourin, M. Couston, C. Deschenes, Methods for Air Admission in Hydroturbines," *the XXIst IAHR Symposium On Hydraulic Machinery and Systems Conference*, 2002, pp. 6–11.

[25] X. Zhou, C. Shi, K. Miyagawa, H. Wu, Effect of modified draft tube with inclined conical diffuser on flow instabilities in Francis turbine, Renew. Energy 172 (2021) 606–617.

[26] Z. Liu, A. Favrel, K. Miyagawa, Effect of the conical diffuser angle on the confined swirling flow induced precessing vortex core, Int. J. Heat Fluid Flow 95 (2022) 108968.

[27] A. Favrel, T. Irie, Y. Ishii, N. Lee, K. Miyagawa, IOP conference series: earth and environmental science, in: Experimental and Numerical Validation of a Francis Turbine Draft Tube Designed for Mitigation of Pressure Fluctuations, IOP Publishing, 2022 012017.

[28] W.-T. Su, M. Binama, Y. Li, Y. Zhao, Study on the method of reducing the pressure fluctuation of hydraulic turbine by optimizing the draft tube pressure distribution, Renew. Energy 162 (2020) 550–560.

[29] C. Tănasă, A. Bosioc, S. Muntean, R. Susan-Resiga, A novel passive method to control the swirling flow with vortex rope from the conical diffuser of hydraulic turbines with fixed blades, Appl. Sci. 9 (22) (2019) 4910.

[30] O. Urban, M. Kurková, F. Pochylý, Mitigation of swirling flow with a vortex rope by passive installations—theory, simulations, and experiments, Phys. Fluids 34 (12) (2022) 124111.

[31] A.I. Bosioc, R. Szakal, C. Tanasa, R.F. Susan-Resiga, Experimental Investigation of a Free Runner Concept Downstream of Francis Turbines," *IOP Conference Series: Earth And Environmental Science*, IOP Publishing, 2022 012018.

[32] Q.S. Wei, Y.D. Choi, B.S. Zhu, Application of J-Groove to the Suppression of Swirl Flow in the Draft Tube of a Francis Hydro Turbine," *IOP Conference Series: Earth And Environmental Science*, IOP Publishing, 2012 022017.

[33] K.C. Anup, Y.H. Lee, B. Thapa, CFD study on prediction of vortex shedding in draft tube of Francis turbine and vortex control techniques, Renew. Energy 86 (2016) 1406–1421.

[34] Z. Chen, P.M. Singh, Y.-D. Choi, Suppression of unsteady swirl flow in the draft tube of a Francis hydro turbine model using J-groove, J. Mech. Sci. Technol. 31 (2017) 5813–5820.

[35] X. Zhou, H. Wu, C. Shi, Numerical and experimental investigation of the effect of baffles on flow instabilities in a Francis turbine draft tube under partial load conditions, Adv. Mech. Eng. 11 (1) (2019) 1687814018824468.

[36] J. Joy, M. Raisee, M.J. Cervantes, A novel guide vane system design to mitigate rotating vortex rope in high head Francis model turbine, International Journal of fluid machinery and systems 15 (2) (2022) 188–209.

[37] J. Joy, M. Raisee, M.J. Cervantes, Hydraulic performance of a Francis turbine with a variable draft tube guide vane system to mitigate pressure pulsations, Energies 15 (18) (2022) 6542.

[38] J. Joy, M. Raisee, M.J. Cervantes, Experimental investigation of an adjustable guide vane system in a Francis turbine draft tube at Part Load operation, Renew. Energy 210 (2023) 737–750.

[39] S. Shiraghaee, J. Sundström, M. Raisee, M.J. Cervantes, An experimental investigation on the effects of cylindrical rods in a draft tube at Part Load operation in down-scale turbine, in: IOP Conference Series: Earth and Environmental Science, IOP Publishing, 2022 012007.

[40] J. Kurokawa, S.L. Saha, J. Matsui, T. Kitahora, A new passive device to suppress several instabilities in turbomachines by use of J-grooves, in: Proceeding of US-Japan Seminar: Abnormal Flow Phenomena in Turbomachines, Nov. 1-6, 1998, Osaka, Japan, 1998, pp. 1–7.

[41] Q.S. Wei, Y.-D. Choi, The Optimization of J-Groove Shape in the Draft Tube of a Francis Turbine to Suppress the Draft Surge," *IOP Conference Series: Materials Science And Engineering*, IOP Publishing, 2013 052030.

[42] S. Shiraghaee, J. Sundström, M. Raisee, M.J. Cervantes, Experimental investigation of Part Load vortex rope mitigation with rod protrusion in an axial turbine, J Fluids Eng (2024) 1–72.

[43] A.T. Favrel, Dynamics of the Cavitation Precessing Vortex Rope for Francis Turbines at Part Load Operating Conditions, EPFL, 2016.

[44] S. Shiraghaee, J. Sundström, M. Raisee, M.J. Cervantes, Characterization of the rotating vortex rope pressure oscillations in a kaplan model turbine draft tube, International Journal of Fluid Machinery and Systems 16 (2) (2023) 204–218.
[45] J.S. Bendat, A.G. Piersol, Random Data: Analysis and Measurement Procedures, John Wiley & Sons, 2011.
[46] P. Welch, The use of fast fourier transform for the estimation of power spectra: a method based on time averaging over short, modified periodograms, IEEE Trans. Audio Electroacoust. 15 (2) (1967) 70–73.
[47] H. Tennekes, J.L. Lumley, A First Course in Turbulence, MIT press, 1972.
[48] G. Krivchenko, Hydraulic Machines, Turbines and pumps, 1994, pp. 368–369.

Nomenclature

Parameters

A: Surface area (m^2)
C: Magnitude-squared coherence (−)
D: Runner diameter (m)
f: Frequency (Hz)
g: Gravitational acceleration (m/s^2)
G: Spectral density (−)
H: Turbine net head (m)
L: Protrusion length (m)
P: Pressure (Pa)
Q: Flow rate (m^3/s)
R: Radius (m)
t: Time (s)

Greek symbols

α: Guide vane angle (°)
β: Runner blade angle (°)
Δ: Difference (−)
Γ: Circulation (m^2/s)
η: Efficiency (%)
ρ: Density (kg/ m^3)
φ: Phase (°)
ω: Angular velocity (rad/s)

Subscripts, Superscripts, and Operators

A: Section A
B: Section B
BEP: Best efficiency point
BPF: Bandpass filtered
DT: Draft tube
ed: Unit specific hydraulic energy and diameter
$L0$: Zero protrusion length
n: Runner
p: Plunging mode
r: Rotating mode
RVR: Rotating vortex rope
$\grave{}$: Signal fluctuating part
$\bar{}$: Time-averaged
$*$: Normalized